Determination of the key structural factors affecting permeability and selectivity of PAN and PES polymeric filtration membranes using 3D FIB/SEM

Helene Roberge, Philippe Moreau, Estelle Couallier, Patricia Abellan

Journal of Membrane Science 653 (2022) 120530

Contents lists available at ScienceDirect

Journal of Membrane Science

journal homepage: www.elsevier.com/locate/memsci

Determination of the key structural factors affecting permeability and selectivity of PAN and PES polymeric filtration membranes using 3D FIB/SEM

Helene Roberge [a,b], Philippe Moreau [a], Estelle Couallier [b,**], Patricia Abellan [a,*]

[a] Nantes Université, CNRS, Institut des Matériaux de Nantes Jean Rouxel, IMN, F-44000, Nantes, France
[b] Nantes Université, CNRS, ONIRIS, Laboratoire de Génie des Procédés, Environnement et Agroalimentaire, GEPEA, F-44600, Saint Nazaire, France

ARTICLE INFO

Keywords:
3D FIB/SEM
3D reconstruction
Filtration membrane
Selective layer
Pore structure

ABSTRACT

Microfiltration (MF) and ultrafiltration (UF) processes are well known in water treatment or separation of valuable biomolecules. They have recently been adapted for microalgae valorization, where filtration employing nanoporous polymer membranes is used to separate and recover lipids and proteins from microalgae extracts. As the design of novel MF and UF membranes with optimized filtration performance (reduced fouling of molecules and increased filtrate fluxes) is leading to increasingly complex pore structures, new characterization methods of filtration membranes are needed. A detailed, nanometer scale, characterization of the three-dimensional pore structure of the membranes and the precise elucidation of the membrane' structure-performance relationship is thus essential for advancing the development of efficient filtration process operating but also novel MF and UF membranes. In this work, the structural features determining the filtration performances of commercially available polyacrylonitrile (PAN) UF and polyethersulfone (PES) MF membranes are determined using scanning electron microscopy (SEM) coupled with a focused ion beam (FIB) at low electron-doses to produce 3D reconstructions with up to 5 nm resolution. Here, methods to identify key structural parameters of the selective layer or skin of the membranes and to estimate the percentage of blind (dead-end) pores communicating with the membrane surface but not crossing the membrane are presented. Furthermore, the data obtained also indicates that widely used models such as Hagen-Poiseuille equation are insufficient to fully describe asymmetric membranes defined by the presence of a thin selective layer. This work opens up the possibility of providing detailed information, useful not only to illustrate novel filtration membrane designs, but also as input data for more complete nanometer-scale based predictive models.

1. Introduction

Membrane filtration processes allow concentrating, separating or purifying the components from complex mixtures in a liquid phase. Recently, they have been applied to microalgae valorization; a new bioresource [1]. Indeed, microalgae produce a variety of valuable biomolecules that can be used in a wide array of areas, such as pharmaceutical industry (antibiotics), cosmetics (antioxidants), food supplements production (proteins rich in several amino acids) and in the biofuel industry as biodiesel (triglycerides) [2,3]. Ultrafiltration (UF) and microfiltration (MF) polymer membranes have, for example, been used for harvesting [4–6], or to separate and recover polysaccharides, lipids and proteins from ground microalgae aqueous extracts [7]. Among the different types of polymer membranes used for microalgae valorization, polyacrylonitrile (PAN) UF membranes and polyethersulfone (PES) MF membranes are commercially available and widely used. These two types of filtration membranes have indeed been successfully used for the fractionation of lipids and proteins [7–9]. The PAN is well-suited for lipid filtration thanks to its hydrophilic properties [9] while the PES is widely used for protein fractionation [10].

Strong fouling of PAN as well as PES membranes has been typically observed both at the membrane's surface and into the porous media [11]. Although membrane fouling is currently considered the major bottleneck for the enhancement of biomolecules' fractionation

* Corresponding author.
** Corresponding author.
E-mail addresses: estelle.couallier@univ-nantes.fr (E. Couallier), Patricia.Abellan@cnrs-imn.fr (P. Abellan).

https://doi.org/10.1016/j.memsci.2022.120530
Received 30 November 2021; Received in revised form 24 March 2022; Accepted 29 March 2022
Available online 1 April 2022

efficiency, understanding the relationship between fouling and membrane structure remains a considerable challenge in the field. It has been demonstrated [12], particularly for PES membranes [13], that depending on the specific surface and pore structure of the membrane, reduced fouling and higher filtrate fluxes can be achieved. In fact, the design of novel membrane structures with optimized filtration performance leads to an increasing complexity of the final pore structures [14]. A detailed characterization of the pores and the precise elucidation of the membrane structure-performance relationship are thus essential for advancing the development of efficient filtration processes and novel MF and UF membranes; not only for membrane processes for microalgae valorization but also for the fractionation of other renewable bioresources.

UF and MF membranes made from polymers have a complex morphology, which varies as a function of depth. They consist in a *selective layer* or *skin*, directly in contact with the fluid to be filtered, above a second porous layer structure with a very high porosity and large pores, settled on a fibrous layer providing mechanical support [15]. The membrane filtration performances (described by its permeability and selectivity) are determined by such *selective layer*. *Remigy and Desclaux* [17] state that both the selective layer (specific thickness with the smallest pores and close to the membrane surface) and the selective "skin" (thinnest layer including only the top most pores connected to the membrane surface) are present in UF and MF membranes. Although the selective layer is responsible for the filtration process efficiency, the morphology of the pores connected to it also has a role to play. Indeed, during the filtration process, three possibilities can be envisioned: i) a pore connected with the membrane surface and that goes through the selective layer (open pore); ii) a pore connected with the surface but not opened at the other end of the selective layer (blind or dead-end pore); iii) a pore not connected with the surface membrane, and thus not connected with the surroundings (closed pores). The latter would include either pores that are closed at both ends or that are only closed at the surface end. It should be noted that while the open pores, situation i), will participate in the filtration process, blind pores, in situation ii), will most likely be clogged by biomolecules and thus only contribute to increasing fouling. Closed pores, in situation iii), will participate neither in the filtration process, nor in the fouling increase. Characterization techniques able of providing 3D information as a function of depth and with enough spatial resolution to identify and fully describe the pore characteristics of the selective layer are thus essential to a detailed understanding of the fouling process. To the best of our knowledge, no experimental nm-scale characterization of the selective layer and its 3D pore structure has been reported for neither MF nor UF membranes.

The selectivity of a membrane depends on the pore diameter at the membrane selective layer surface and on the affinity of the biomolecules towards the polymer. The permeability of the solvent (water in this case) through the membrane can be determined using simple widely applied models, such as the Hagen-Poiseuille equation (H–P model, see supporting information for an introduction to this model and its application to the membranes), by assuming a homogeneous material where the pores are perfect cylinders, identical and completely unblocked. This model fails for the case of real asymmetric membranes, where some of the pores can be blocked, connected in complicated ways and present a complex morphology. According to *Mostaghimi et al* [18] and *Song et al* [19], the H–P model can strongly overestimate permeability by a factor of 10 or more, particularly for the more heterogeneous porous media. The H–P model considers a convective flow through pores, but it doesn't take into account several questions ([20,21]): the interaction between the solvent and the membrane through the surface tension, the wettability, which can impact the capillary pressure, the polarity of membrane and solvent, which can induce the formation of layers of solvent molecules and a reduction of the effective pore radius; the properties of the fluid in micro or nanopores (effective viscosity), the possible difference from the laminar classical flow due to different slip boundary conditions. More complicated models are being developed. The processes by which fouling occurs are complex and depend on structural factors such as the membrane porosity or pore connectivity, as proven for protein fouling [22]. The input for such more detailed models requires precise information at the nanometer scale, which has not been available so far. The output of high resolution 3D characterizations could serve as such input [17,23].

Generally, porous polymer materials used as filtration membranes are characterized using large-scale indirect measurements of their pores e.g. by porosimetry [24]. Scanning electron microscopy (SEM) allows for a direct visualisation of material structure and has typically been used for either surface or cross-section 2D imaging [25,26]. Pores, however, are 3D structures and require 3D characterization and quantification methods for a full description. In addition, 2D image SEM analysis presents limitations for quantifying the amount of pores that truly participate to the filtration process, since a quantitative estimation of blind and closed pores necessitates 3D data.

Serial sectioning and imaging using dual beams (Focused ion beam, FIB/SEM) [27–31] or an ultramicrotome mounted in the SEM chamber (Serial block face, SBF) [32] allows the 3D reconstruction of the membrane structure. The 3D structure of a membrane can be reconstructed from the stack of 2D images. Then, 3D models allow characterisation of several parameters of interest, such as the pore size, the porosity or the connectivity [24,27]. Typically, SBF provides a worse resolution than FIB/SEM. As demonstrated by *Reingruber et al* [32], working on a PES flat sheet membrane with a nominal pore size between 0,45 and 0,60 μm, the resolution achieved by SBF (non-cubic voxel size $25 \times 25 \times 50$ nm^3 in their case) is insufficient for membranes with a pore size below 200 nm. In addition, this technique requires embedding the sample in a resin to allow it to be cut by the ultramicrotome placed in the SEM and therefore, it is not possible to perform SBF on non-embedded samples. Experiments on nanoporous materials when characterized in 3D using a SEM coupled with a focused ion beam (FIB), allow for a superior resolution (down to 3–5 nm in cubic voxel size; pixel size and thickness slice [16,30,31]) with a field of view of a few micrometres (e.g., Prill et al. [31] use a field of view of 3.4×2.7 μm). The application of 3D FIB/SEM in nanoporous polymer materials is now expanding, with examples in polymer electrolyte fuel cells (PEFCs) [30] or porous polymeric particles [21]. Regarding filtration membranes, *Kłosowski* et al. [33] used 3D FIB/SEM technique on reverse osmosis (RO) membranes to enable the characterisation of key structural properties. *Prill* et al. [31] used the technique on ZrO_2 Al_2O_3 nanoporous ceramic membrane as a 3D image support of fluid permeability simulation. However, this technique is still rarely employed for MF and UF polymeric filtration membranes. *Brickey* et al. [16] very recently performed FIB-SEM on membranes (virus filtration applications). Their samples do, however, not present the layered porous structure characterising UF and MF membranes and their method is not aimed and suited to identify a possible selective layer. Studies characterizing block copolymers [27,29] remain the closest to UF and MF polymeric membranes samples. *Sundaramoorthi* et al. [27] were among the first to use 3D FIB/SEM on porous block copolymer membranes and to obtain a complete mapping of porosity, connectivity and average pore size in different layers. However, the authors explore a block copolymer sample, which, because of its fragility, cannot be used as a flat sheet commercial UF and MF membrane [34]. Moreover, the use of a large thickness slice (50 nm) is not sufficient to characterize the selective layer pore structure of PAN or PES filtration membranes.

The utilization of 3D FIB/SEM for MF and UF filtration membrane characterisation present a number of important technical challenges. Firstly, polymeric membranes consist of amorphous materials presenting little contrast and a strong sensitivity to the electron and ion beams, making sample imaging challenging [28,33]. The use of FIB/SEM in 3D acquisition for such materials requires rigorous control and optimization of the experimental parameters, such as beam energy, current or dwell time for both types of beams [27,29]. It is in fact essential to avoid damage to the sample and charging effects that result in continuous sample drift and a loss of information during the data reconstruction. In

order to study block copolymers, *Nunes* et al. [29] and *Sundaramoorthi* et al. [27] were only able to obtain a 3D reconstruction (15 and 8 nm resolution, respectively) after adapting all beam parameters. Such parameters are material and sample preparation dependent and must be optimized and reported for each specific case. In that sense, PAN and PES filtration membranes are no exception and their study by FIB/SEM requires additional care and control of the experimental parameters to avoid sample damaging and charging.

Another technical challenge that must be considered for the study of the 3D structure of the UF and MF membranes is the presence of the shine-through artefact in the 3D reconstructions. This is a common issue of porous media 3D reconstruction [30,31,35] and it is due to the fact that material from subsequent slices is imaged through the pores, and this leads to a deformation of the reconstructed pores along the FIB-milling direction. In order to remove the shine-through artefact, Terao et al. [30], working on porous media for polymer electrolyte fuel cells, developed with success a novel image processing technique, using ESB (Energy Selective Backscattered) images to complement information of SE (Secondary Electron) images and obtain segmentation maintaining the inner surface of the cross section as a solid area. However, such a method requires extensive programming and data processing developments to be adapted to each type of membrane. A loss of generality and transferability could thus be envisaged if various types of membranes are to be compared. An empirical method, consisting of filling the pores using epoxy resin in order to minimize the effect of the shine-through artefact has also been reported [30,36]. As an example, *Iwai* et al. [36], decided to fill the pores of a solid oxide fuel cell (SOFC), allowing to image only the edge of the pores and therefore removing the shine-through artefact. At the same time, they improved the pore segmentation process, since pores appeared as a homogeneous black region without contrast gradient. This method, however, presents limitations when characterizing polymer porous materials, the main issue being the low contrast between the polymer membrane and the resin, as both are polymer materials. Nonetheless, resin embedding is already used for the characterization of polymer filtration membranes: *Reingruber* et al. [32] embedded a PES flat sheet filtration membrane to perform SBF and obtained relatively good contrast. And, at the same time, they avoided the shine-through artefact even though this was not detailed in the manuscript which precludes any conclusion on the pros and cons of the method. So far, resin embedding has not been applied to PAN membranes.

In the present study, the selective layer of PES and PAN filtration membranes is characterized. A distinction between the "selective layer" and the "skin" based on the analysis of the pore structure as a function of depth is performed. Also, an identification of the percentage of surface pores which are open pores and the percentage of blind pores is shown. The extraction of the 3D information allows for the quantification of several parameters of interest, within the same experiment, such as pore size, porosity and connectivity [29]. The 3D quantification of pores, by integrating the third direction of the object, reduces the measurement error and avoids the need for estimation from a 2D image in comparison with other techniques (e.g. 2D cross section, porosimetry). Conditions to analyse the membranes without damaging them are found and a comparison of the results obtained after the resin embedding of PES and PAN to the data measured with the shine-through artefact is presented. All microscope parameters in order to carry out these experiments while preserving a 5–10 nm of resolution for the smallest pores characterization are provided. This high resolution provides the possibility of producing information that can directly feed detailed models for fouling, permeability and selectivity of filtration membranes using molecular dynamics, DFT, finite elements, among others.

2. Experimental

2.1. Materials

2.1.1. Polymer filtration membranes

Two types of flat-sheet commercial filtration membranes were analysed: a polyethersulfone (PES) microfiltration membrane with an average nominal pore diameter of 0.1 μm (Koch membrane systems, USA) and a polyacrylonitrile (PAN) ultrafiltration membrane (Orelis, France) with a molecular weight cut-off of 500 kDa (nominal 30 nm mean pore diameter).

2.1.2. Conditioning of PES and PAN membranes

All filtration membranes were conditioned prior to their characterization, following the procedure initially reported by *Rouquié et al* [37] for pilot-scale membrane cleaning and compaction: using a cross-flow filtration module (Rayflow X100, Orelis-Novasep, France) the membranes were cleaned with an alkaline solution containing bleach (pH10-11) followed by Ultrasil 100 solution. They were carefully rinsed with softened water at intermediate steps and finally rinsed with ultrapure water. They were compacted at 2 bar until stable flux was achieved. Flux values were 200–250 and 70 $L \bullet h^{-1} \bullet m^{-2}$ at 1 bar of transmembrane pressure for PES and PAN membranes, respectively, and are in good agreement with expected values given by the manufacturers.

2.2. Electron microscopy characterization and sample preparation

2.2.1. Membrane preparation for electron microscopy

All membranes investigated by FIB/SEM were stained to increase image contrast. Ruthenium tetroxide (RuO_4) was used as a staining agent for PES membranes, following Trent et al. (1982) [38]. Phosphotungstic acid (PTA) was used as a staining agent for PAN membranes due to its affinity to nitrile groups, as proposed by Chen et al. (2005) [39]. Neither ruthenium tetroxide (RuO_4), nor osmium tetroxide (OsO_4) provided sufficient contrast in the case of PAN and they were consequently ruled out. The membranes were fully immersed in a staining solution (1% in water) for 1 h, then rinsed. Staining was followed by a few days of dehydration in a heat chamber at 35–40 °C until a constant mass was obtained. Half of the samples presented in this work underwent an additional step consisting in embedding the membranes into an acrylic resin (LR White Resin, LFG distribution, France), which polymerises at 60 °C during 48 h. All membranes, embedded and non-embedded (henceforth termed "empty membranes"), were fixed on a SEM mount and metallised by carbon thread evaporation (CED 030 Carbon Thread Evaporation Device – BALTEC) leading to an approximate 25 nm layer of carbon to render their surface conductive.

2.2.2. 3D FIB/SEM data acquisition

Data acquisition for 3D reconstructions were carried out using a FIB/SEM ZEISS Cross Beam 550 L assisted by Atlas 5 ZEISS software (See the detailed procedure in the supporting information).

3D FIB/SEM data acquisitions were performed on PES and PAN membranes with (embedded volume) and without (empty volume) resin embedding. Data were acquired using the experimental conditions shown in Table 1. The voxel resolution of 3D data was set to be cubic (equal value for X, Y and the slice width Z) and with a side size of 5 nm for PAN and 10 nm for PES membranes. According to the Shannon's theorem [40], a detectable object must have a size larger than at least twice the minimum pixel size and thus, at least 2 pixels are needed for a pore to be detected. It should be noted that in this case, for the segmentation of the pores with the voxel sizes given above, the mean size of the pores are at least six times larger than the pixel sizes. The targeted object was defined as the nominal size of the pores as provided by the manufacturers (30 and 100 nm for PAN and PES, respectively). Two volume acquisitions of different areas within the membranes per preparation condition (empty or embedded samples) and per type of

Table 1
Data acquisition parameters used for 3D FIB/SEM of PES and PAN membranes. [a]Exact values might differ slightly from one volume to another. Nominal pore sizes are those initially provided by the manufacturers.

	PAN membrane (nominal pore size: 30 nm)	PES membrane (nominal pore size: 100 nm)
3D FIB/SEM acquisitions of *empty samples*	2	2
3D FIB/SEM acquisitions of *embedded samples*	2	2
3D volume size[a]	$10 \times 5 \times 5\ \mu m^3$	$15 \times 15 \times 15\ \mu m^3$
Cubic voxel resolution	5 nm	10 nm
Energy and current of SEM observation	2 keV 200 pA	2 keV 200 pA
Electron fluence of *empty sample*	2 e−/Å^2	1.2 e−/Å^2
Electron fluence of *embedded sample*	20 e−/Å^2	3.7 e−/Å^2
Field of view, dwell time and line average of SEM observation	10 μm 4 μs 1	19 μm 15 μs 2
Energy and current of FIB milling	30 keV 300–700 pA	
Acquisition time	24–48 h	

membrane investigated (PES and PAN) were performed. Thus, a total of 8 vol were acquired.

Polymers are well-known for leading to imaging and milling difficulties [41,42]. A major part of this work was thus devoted to find and optimize the main parameters (see the final parameters used in Table 1 and details in the supporting information). As an example, the procedure defined to optimize the ion beam current is presented in the supporting information.

SEM parameters were set to minimize drift (charging effects) while keeping reasonable image quality for subsequent analysis. Secondary electrons (SE) and backscattered electrons (BSE) SEM images were obtained using 2–5 keV primary electrons and 200–1000 pA beam currents, depending on the material and the aimed spatial resolution (see the final parameters and electron fluence values in Table 1 and supporting information). It should be noted that the electron fluence (electron per unit area; historically named *electron dose* in electron microscopy community) used for both the PAN empty (2 e−/Å^2 to reach 5 nm resolution) and PES empty (1.2 e−/Å^2 for 10 nm resolution) membranes are below the electron fluencies reported to keep different polymers under the critical electron fluence values for damage using different measurements such as the fading of spots in electron diffraction patterns or the loss of chemical bonds (carbon and oxygen bonds) [43].

2.2.3. 3D reconstruction and analysis

The Dragonfly software, dedicated to scientific image processing and analysis such as transformation, segmentation and quantification of multi-scale objects in a 2D image or 3D volume, has been developed and commercialized by Object Research Systems Inc, Montreal Canada [44]. It was used to reconstruct and analyse the different stacks of images. Firstly, the raw images in the stacks were aligned relative to one another in order to account for possible drift or errors during acquisition, the module "Slice Registration" was used to that end (see more information about the modules used in support information). Further steps are presented in Fig. 1a. After having acquired the 8 large volumes, three smaller volumes (of identical sizes) near the surface (called triplicates) were extracted from each of them. Triplicates were analysed using parameters shown in Table 2. This procedure allowed us to: (i) avoid pre-processing (filters, binning …) steps typically done to account for local variations on image contrast due to drift, loss of focus or artefacts, in order to limit the loss of information, (ii) better account for local surface roughness variations. Indeed, smaller analysis volumes allowed us to keep surface roughness as low as possible and thus, do a more accurate assignment of the "surface plane" (zero value) for this depth analysis. Finally, (iii), provide an estimate of the homogeneity of the results at this given scale (see supporting information).

The analysis of triplicates (see right hand side of Fig. 1a) provided a set of membrane characteristics (namely pore sizes, volume porosity, pore tortuosity and connectivity) as a function of depth. In practice, each triplicate was divided in smaller volume layers with top and bottom surfaces parallel to the XZ plane (i.e. parallel to the membrane surface), along the Y direction (as shown in Fig. 1b). Each layer overlapped with the next one by 50%, so that the analysis covers the entire membrane structure. Layers have a thickness of 100 and 300 nm for PAN and PES membranes, respectively, and measurements are separated by 50 and 150 nm, respectively. The thicknesses of the layers were chosen so that it was at least 3 times larger than the nominal pore size provided by the manufacturer (100 nm $\geq 3 \times 30$ nm for PAN and 300 nm $\geq 3 \times 100$ nm for PES). Finally, an automated segmentation of membrane pores was done for each layer. This corresponded to the selection of a grey level window in the image histogram with respect to the object of interest, here the pores. A filter was applied to remove all objects smaller than 3 pixels. In general, to account for contrast gradient effects and the sample condition (embedded or not), segmentation was adapted for each individual layer. Based on the pore segmentation volume, the mean pore diameter was estimated (Fig. 1b), defined as the diameter of the largest sphere that fitted within the 3D pore (local thickness in 3D) [41]. The tortuosity, here the ratio of the length of the pore to the distance between its ends (the rectilinear distance between the beginning and the end of the object) and the connectivity were also extracted from the skeleton of the segmented volume (Fig. 1b) (skeletonization process) [42]. Concerning the estimation of blind pores, the Y position (the direction of the depth from the surface membrane) for each pore was identified by using the multi-ROI analysis based on the pore segmentation. Thus, pores connected to the surface as well as their Y position were identified and sorted according to their starting and final Y positions.

3. Results and discussion

3.1. Effect of the "shine through artefact"

It is important to reiterate that most porous media studies are affected by the so-called *shine-through artefact* during 3D data reconstruction. In order to evaluate the effect of this artefact, 3D FIB/SEM volumes of PAN and PES membranes acquired following two different approaches were analysed: 1) using resin to fill in the empty pores of the membranes (*embedded membranes*), which should not be affected by the shine-through artefact and 2) without the resin-embedding step (*empty membranes*), which should suffer from the shine-through artefact.

In Fig. 2 are presented the XY and YZ planes of 3D reconstructed volumes obtained on an empty (Fig. 2a) and an embedded (Fig. 2b) PES filtration membrane. 3D reconstruction was performed from a stack of images acquired using the (in lens) SE and the secondary electrons secondary ions (SESI) detectors, simultaneously. In Fig. 2a, the reconstructed YZ plane shows the clear elongation of pores (indicated by red arrows) in the Z direction. This is characteristic of the shine-through artefact whereby the edges of the pores are imaged (in Z direction), even when contrast arises from depths deeper than the z-slice and it should not be taken into account in the pore segmentation. In the case of the embedded membrane (Fig. 2b), such elongation is not present anymore in the YZ plan. The contrast is, however, clearly diminished. A lower contrast between membrane and resin (embedded pores) as compared to that between the membrane and empty spaces (pores) was expected, since membranes and resins are both polymer-based materials. The loss of contrast and thus, the segmentation difficulty was even more pronounced with PAN membranes (see Fig. 3). As already mentioned, since the shine-through artefact occurs along the Z direction (milling direction), a pore elongation is expected, with possibly an

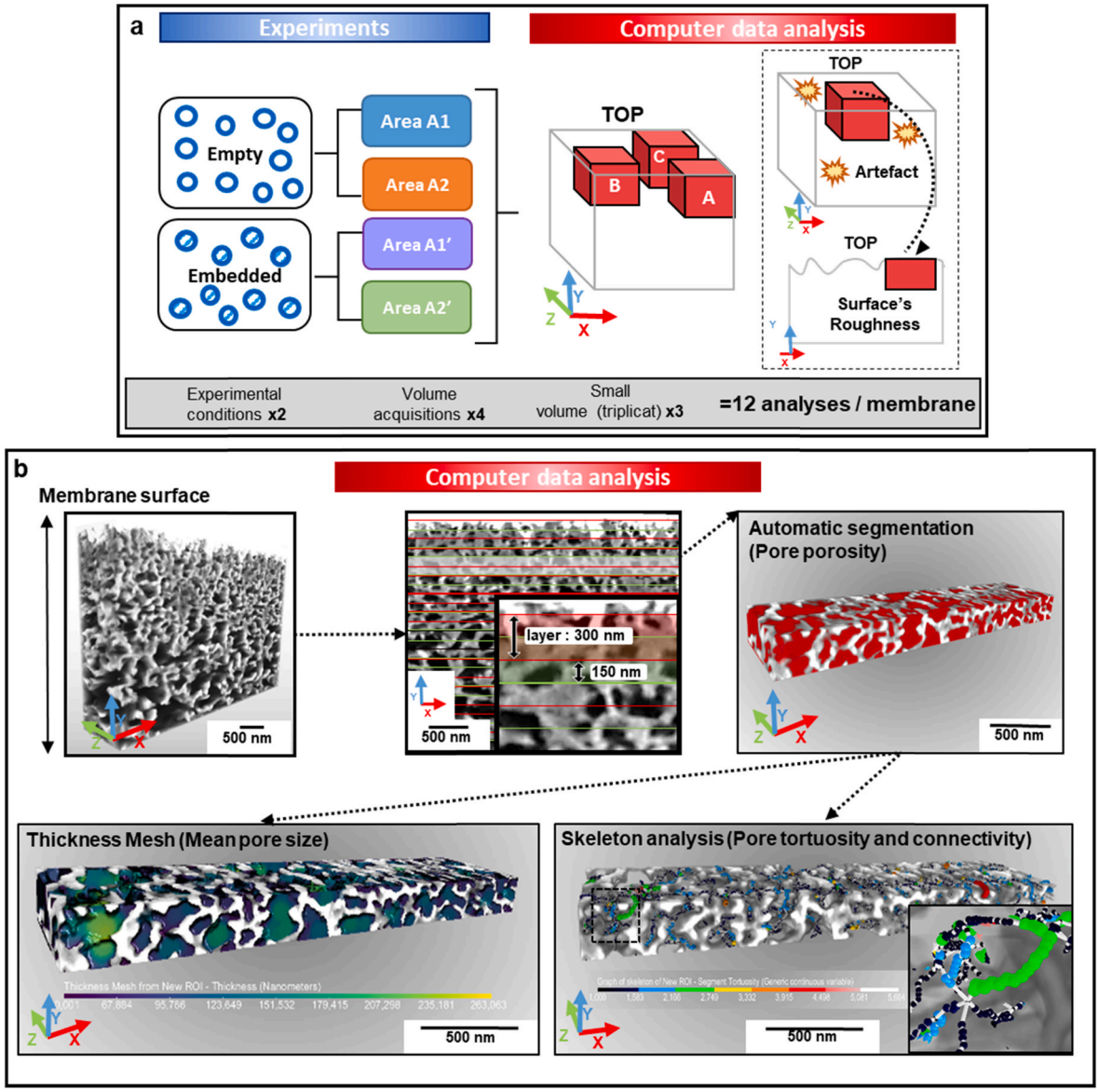

Fig. 1. Illustration of the main 3D analysis steps in the PES membrane as an example. (a) Procedure used in this study to analyse membranes in 3D. For each membrane reference (PAN or PES), two experimental conditions, empty (without resin, blue empty pores) and embedded (with resin, blue filled pores) membranes were studied. For each experimental condition, two different volumes were acquired. In each 3D data acquisition, three 3D smaller volumes (triplicates) were defined and analysed using the Dragonfly® software. (b) analysis of an extracted volume of PES membrane. The extracted volume was divided in layers parallel to the membrane surface. Each layer has a thickness of 300 nm and the distance separating the layers was set to 150 nm. For each layer, pores were segmented in order to extract their volume, the mean pore size, the tortuosity and the connectivity. (For interpretation of the references to colour in this figure legend, the reader is referred to the Web version of this article.)

Table 2
Data analysis parameters used for the 3D reconstructions of the FIB/SEM data of PES and PAN membranes. [a]*this value is explained by the fact that one stack was too small to allow deeper analysis.* Nominal pore sizes are those initially provided by the manufacturers.

	PAN membrane (nominal pore size: 30 nm)	PES membrane (nominal pore size: 100 nm)
Analysed volume[a]	2 × 1 × 1 μm	4 × 3 × 2 μm
Number of analysed layers (in the depth or the Y direction) per triplicate	18[a]-28	20
Thickness of a layer	100 nm	300 nm
Space between layer measurements	50 nm	150 nm

increase in pore size and porosity along the YZ plane of the 3D reconstructed volumes from empty membranes. Because of this one-dimensional effect on the experimental data, its effect on the quantification of the different parameters can be strongly influenced by the quantification procedure of choice. In order to illustrate this, XY and YZ planes are presented in Fig. 2c, where pores are segmented to quantify their size by the local thickness (LT) method using circles. This method is the 2D equivalent of the 3D quantification presented below (see methods section for details). These results were compared with values obtained by using the most commonly used technique to quantify pores size in 2D, i.e. by Feret diameter measurements [45]. The porosity values for both planes are also given.

As shown in the comparison of the means pore size for both 2D quantifications in Fig. 2c, Feret diameter measurements lead to an overestimation of the pore size in the YZ plane, whereas local thickness

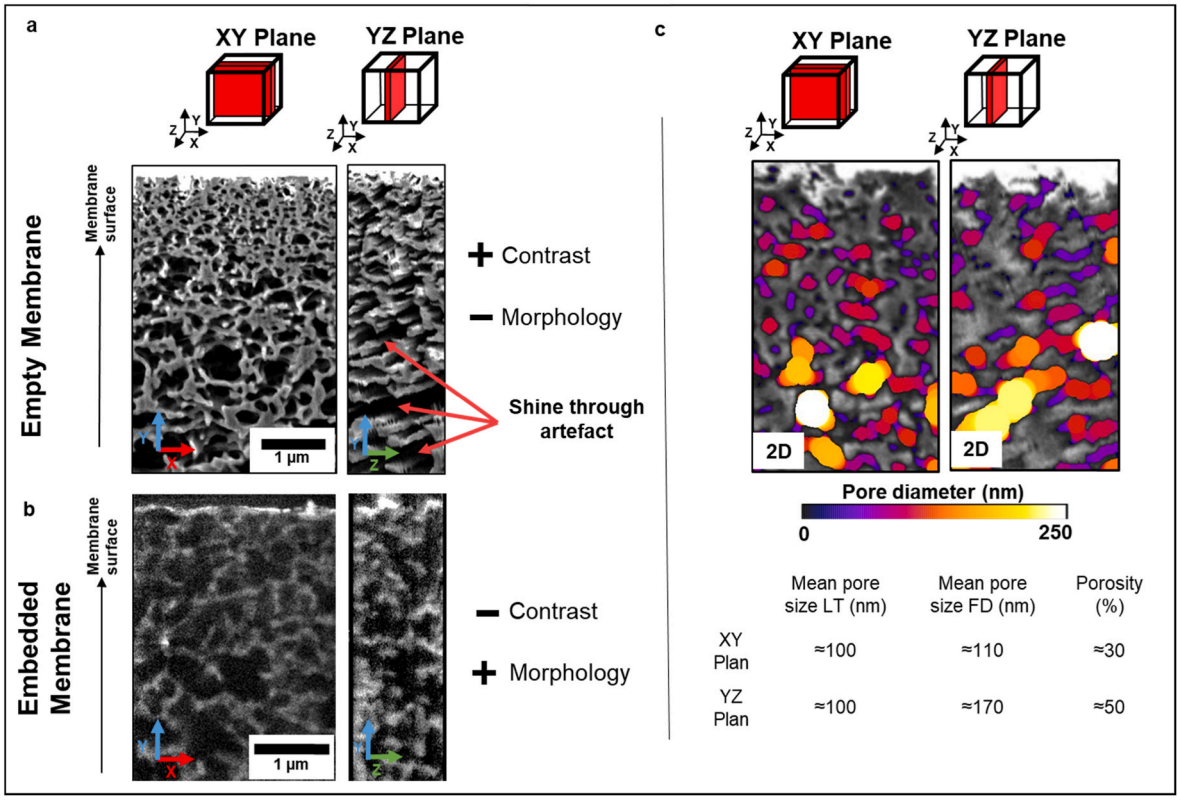

Fig. 2. Illustration and impact of the shine-through artefact in the empty and the embedded PES polymeric membrane. a) The empty membrane presents a good contrast but also morphology issues due to the pore elongation in Z direction (shown by red arrows). b) The embedded membrane presents a lower contrast but a closer to reality morphology. **c**) 2D pore quantifications (coloured areas) for XY and YZ planes of the PES empty membrane (by local thickness measurement with 2D circles). Mean pore sizes, by local thickness (LT) and mean Feret diameter (FD) measurements, and porosity extracted from the 2D segmentation on both planes corresponding to an area of 1003 × 1675 nm^2. (For interpretation of the references to colour in this figure legend, the reader is referred to the Web version of this article.)

measurements yielded the same values for the mean pore sizes along the two perpendicular planes. The same discrepancy, however, is observed for both quantification procedures applied to the estimation of the porosity values along the different planes, Therefore, when using local thickness for the 2D pore quantification of the PES membrane, a minor impact of the shine-through artefact on the mean pore size, is demonstrated. This finding confirms the choice of local thickness in 3D as the preferred method for 3D FIB/SEM data analysis of empty membranes. These results were confirmed in the case of PAN empty membranes (not shown). The shine-through artefact leads to an overestimation of the porosity (from 30% in the XY plane to 50% in the YZ plane as shown in Fig. 2c), depending on the orientation of the pores parallel or not to the Z axis. The porosity increase is more important when large pores are present, because they take part in a larger number of FIB slices. This increase should be constant for a specific pore size and for a specific depth in the material, thus the trend of the porosity with depth, if merely dependent on the shine-through artefact, should follow the pore size variation. In other words, the data shown suggests that a modification of the structure that leads to a discontinuous rise of the porosity should not be affected by the shine-through, even if the porosity may be somehow overestimated.

In order to limit the shine-through artefact, embedding of the membranes was performed. However, the loss of contrast between the polymer membrane and the resin had a negative impact on the efficiency of the image segmentation. This was particularly true for the PAN membranes. The 3D reconstruction of the empty and embedded membranes are detailed in the following paragraph and Fig. 3 illustrates this difficulty. Moreover, the embedding of the membranes led to the swelling of the porous media. This phenomenon was critical for the PES membrane (see the supporting information), and had a strong impact on the structural parameters quantification (see the following paragraphs).

These are two redhibitory defaults for the embedding technique. This is the reason why empty and embedded membranes analyses were systematically compared. Despite the shine-through artefact and considering the limited impact on the pore diameters and on the trends of the porosity, the analyses allowed us signalling to a discontinuity along the porous media depth.

3.2. 3D visualisation of PAN and PES membranes

Fig. 3 shows 3D volumes of PES and PAN membranes acquired by 3D FIB/SEM after reconstruction. Both membranes are presented for empty and embedded conditions. In Fig. 3a, the PES membrane offers a high and uniform contrast from the surface to the bottom of the membrane. Such is not the case for the PAN membrane (Fig. 3b.), where a large contrast variation along the Y axis (depth) is observed. As explained before, the contrast of the embedded membranes is much lower than of the empty membranes. These latter cases led to a more challenging pore segmentation, especially for the PAN membrane. These qualitative considerations explain why error bars presented in the next section show a strong variability in magnitude. As will be demonstrated in the next section, the pore quantification of the embedded PAN and PES membranes reveal higher values in pore size and porosity compared to those for empty membranes. Consequently, in agreement with the evaluation of the shine-through artefact presented above, it was decided to base this study on empty membranes (both types), while keeping the embedded membranes as an additional set for comparison.

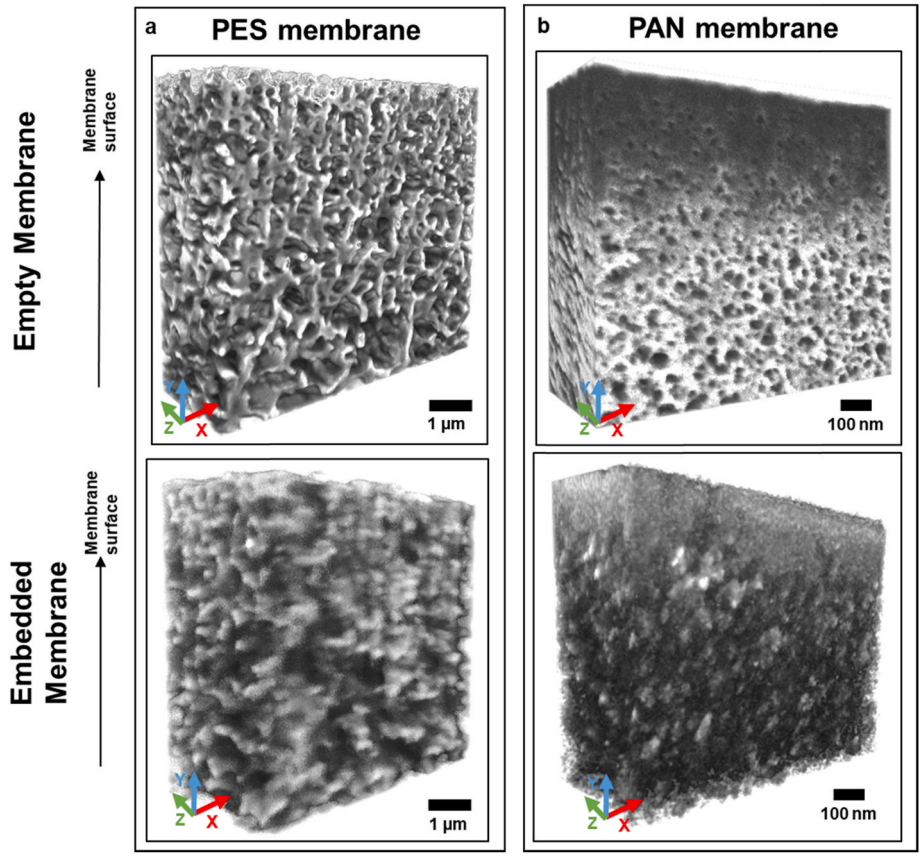

Fig. 3. 3D visualisation of (a) PAN and (b) PES membranes, respectively, with 5 nm and 10 nm resolutions. Volumes obtained by 3D FIB/SEM for empty (upper images) and embedded (lower images) membranes using the SESI detector.

3.3. Determination of selective layer thicknesses for PAN membranes

For the PAN membrane, in Fig. 4, the mean pore size (4a), porosity (4b) and tortuosity (4c) of pores are presented for empty (green points) and embedded (black points) PAN membranes, from the surface to a 1400 nm depth. The values presented are the average over 6 analysed volumes (two sets of triplicates; see details of the quantification in the methods section). The error bars take into account standard deviation (see the individual values measured for each parameter in the supporting information). A schematic view of the proposed pore structure of the PAN membrane as a function of depth is presented in Fig. 5. It should be stressed that these measurements showed high repeatability (see supporting information for the individual values measured at the six different volumes analysed for PAN membranes). According to the observations from the empty PAN membrane, the pore diameter and the tortuosity rise slowly and steadily from the surface of the membrane to the inner most porous media. Concerning the porosity, it is rather stable from the surface to about 505 nm (Fig. 4b.), before a monotonous and faster increase occurs. The porosity is directly linked to the size and the number of pores. Since the size of the pores do not show a similar change in slope, these observations are indicative of a sharp increase in the number of pores from depths of about 505 nm. These observations

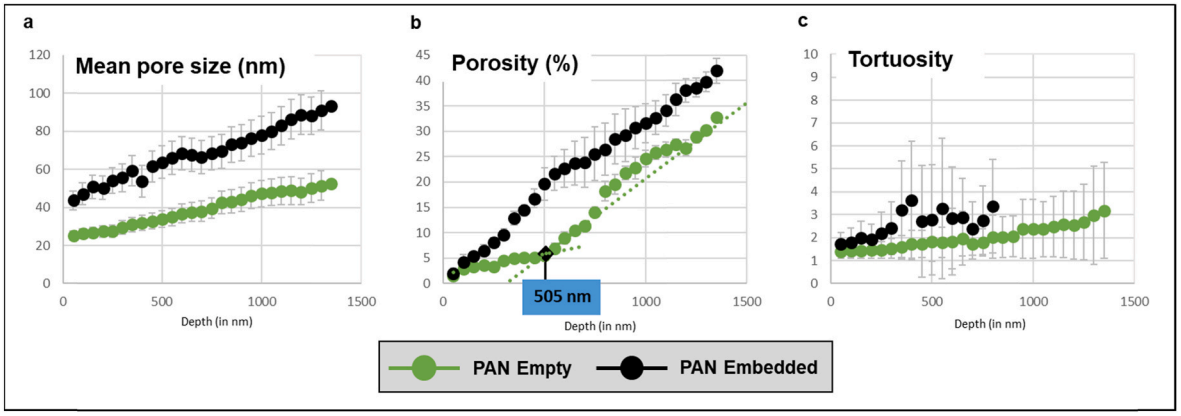

Fig. 4. 3D quantification of pore structural properties for the PAN membranes (empty in green, embedded in black) from the top surface to the bottom of the volume (Y direction). Mean pore size (4a), porosity (4b) and tortuosity (4c) of pores according to the depth. (For interpretation of the references to colour in this figure legend, the reader is referred to the Web version of this article.)

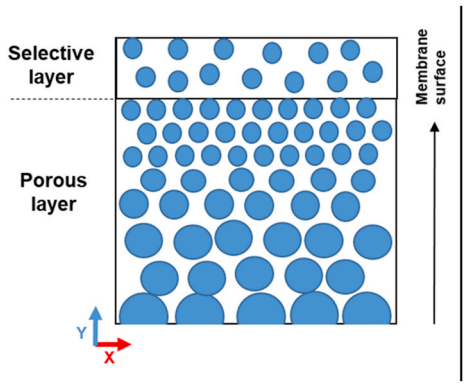

Fig. 5. Schematic illustration of a cross-sectional view showing the morphology of the membrane, including the selective layer (of 505 nm thickness) highlighted in the porosity quantification.

reveal a region near the surface constituted of sparse number of pores with a limited rise of their diameter (25–35 nm), followed by a region with a higher number of pores. Overall, two distinct regions are evidenced, with distinct pore diameter ranges: a selective layer is identified whose thickness can be estimated to be 505 nm.

The selective layer determines the intrinsic permeability of a membrane. Thanks to the measurements of pore sizes (d), porosity (ε) and tortuosity (τ), and using the H–P model, the calculated intrinsic permeability K can be estimated and plotted (see supporting information). It follows the same evolution as the porosity: minimal and stable between the surface and 505 nm in depth, before a steady and monotonous increase. These results on the porosity and the calculated intrinsic permeability confirm the presence of a selective layer and its thickness of 505 nm as represented on the schematic view of Fig. 5.

The transition between the two porosity regimes is not as clear for the embedded PAN membrane. It should be noted that quantification would not be as consistent as for the empty one (see supporting Figs. S4 and S5 for a comparison between individual volumes analysed). The delicate process of resin embedding explains the larger dispersion of the results observed for embedded membranes (see pore size graph in Supporting information), hence a smoother transition between the two regions. As already mentioned, macroscopic measurements using optical microscopy were performed and are consistent with the assumption of a swelling effect by the embedding process (see Table S1 in the supporting information). Even though both sample preparation protocols: based on either dehydration or resin embedding will surely have an effect on the structural parameters of the membranes, the macroscopic measurements performed suggest that resin embedding changes the pore size the most as compared to fully hydrated membranes. The occurrence of an overall expansion of the pores when the resin fills in the membrane is observed. How this evolution affects the membrane pores for different depths considered remains however unknown.

3.4. Determination of selective layer thicknesses for PES membranes

The same procedure was applied to the determination of the selective layer thickness for the PES membrane. First of all, as for the PAN membrane, values (see in supporting information) show relatively small variations from one analysed area to another. These measurements prove a certain degree of homogeneity of the membrane (in Y and Z directions) hence a strong confidence in the conclusions. In Fig. 6 mean pore size (6a), porosity (6b) and tortuosity of pores (6c) are presented for empty (pink points) and embedded (blue points) PES membranes as a function of depth from the surface to a 3000 nm depth. Averaged values were obtained over the 6 vol analysed per sample (see in supporting information). According to analyses of the empty PES membranes, steady increases of the tortuosity and of the mean pore size were observed without any strong change of the slope. Following the same considerations as those described for the PAN membranes, the averaged intrinsic permeability was calculated using H–P model for empty and embedded membranes as a function of depth (see Supporting information). It present a steady increase without any strong slope change. The minima of porosity (Fig. 6b) and permeability K (Supporting information) are localised at, or close to the surface of the PES membrane. Either a sharp increase of the permeability near the surface or a steady increase with depth is indicative of a very thin selective layer. At least, it should be smaller than the distance between two successive analysis layers, i.e. 150 nm (in the Y direction). In the literature, this picture is in fact often called a *selective skin* [23,37]. A schematic view of the proposed membrane structure is presented in Fig. 7b. This detailed quantitative study of the 3D volumes of both types of membranes is confirmed by the qualitative visualisation of respective cross sections (Fig. S6).

Two very different membrane structures were thus identified: a selective layer of ~500 nm for PAN and a skin for PES, matching with a thickness comprised between 60 nm (estimated mean pore size) and 150 nm (the depth analysis step).

In order to check how consistent these results are with macroscopic measurements, flow calculations were performed using quantitative 3D structural analyses and compared to experimental data (see supporting information). There are some important considerations to take into account when performing such comparison. First of all, it must be mentioned that flow calculations in membranes typically present a wide variability, inherent to the material, which has been reported by other authors [7,12,46]. Furthermore, it should be reminded that the Hagen-Poiseuille law is not based on a nanometer scale description of

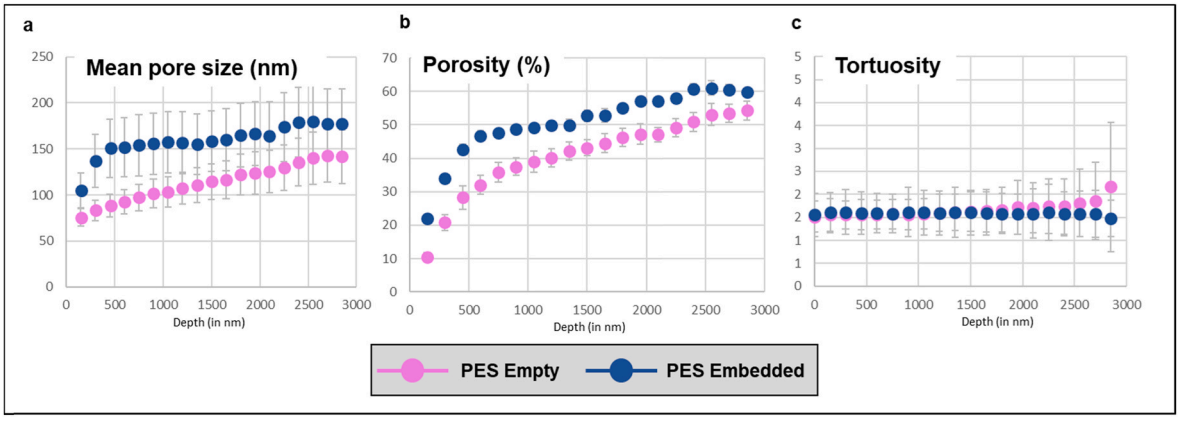

Fig. 6. Quantification of pore structural properties of the PES membrane from the top surface to the bottom of the volume (Y direction). Mean pore size (6a), porosity (6b) and tortuosity (6c) of pores as a function of the depth.

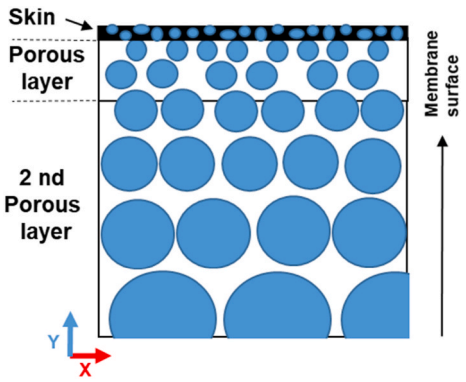

Fig. 7. (a) Intrinsic permeability (depending on the mean pore size, the porosity and the tortuosity) of the PES membrane from the top surface to the end of the volume (Y direction). (b) Schematic cross-sectional view of the membrane morphology.

membranes and does not take into account the impact of the interaction between the membrane material and the solvent (Marchetti 2012 [20] et Chen 2017 [21]). In particular, the membrane wettability or hydrophobicity (PAN membranes are often more hydrophilic than PES membranes) might also play a role on the measured flow [47,48]. [12, 46]The macroscale flux measurements are compared with those calculated for PAN and PES (empty and embedded) membranes using the Hagen-Poiseuille law for a water viscosity at 20 °C and a transmembrane pressure of 1 bar in supporting information (Tables S2 and S3). For empty conditions, the H–P model overestimates the permeability by a factor of 7 for the PAN membrane (measured flux: **70** L • h^{-1} • m^{-2}, calculated flux: **535** L • h^{-1} • m^{-2}) and 50 for the PES membrane (measured flux: **250** L • h^{-1} • m^{-2}, calculated flux: **13 500** L • h^{-1} • m^{-2}). This difference corresponds to the one noted in literature [19]. An even larger discrepancy was found for the embedded membranes. Here is suggested that either the model used and/or the experimental microscopic parameters are not sufficient to describe the flux through the selective layers and that factors such as the polymer hydrophobicity or the local chemistry that may also influence the flux must be taken into account. However, the microscopic description of the porous media in this manuscript gives access to data needed for developing more elaborated models.

3.5. Estimation of blind pores and limits of 2D SEM analysis of pore sizes and number

Quantification of pore sizes as revealed by 2D SEM give mean pore diameters of 20 nm and 90 nm for PAN and PES membranes, respectively (supporting information). The associated surface porosities correspond to 7% and 6%, respectively. These results are close to those obtained for small depths when 3D pore quantification is performed (Figs. 4 and 6). Differences could be explained by the sputtered platinum, necessary for the observation of insulating samples, which could have a noticeable impact on the surface analysis. 2D pore quantification with SEM is much more widespread and less time consuming [3] than the 3D pore quantification method but the latter provides a whole set of new information.

In this part, 3D reconstructions and pore quantification were used to analyse the pore efficiency in the filtration process, by estimating the amount of surface pores allowing a flow through the selective layer or skin, thus the number of open pores. Fig. 8 presents 3D visualisations of the surface-connected pore going through either the selective layer or skin in PAN and PES membranes. Pores connected to the surface are shown in purple colour. 99% of pores at the PES surface cross the selective skin (60–100 nm thick), whereas only 75% of pores at the PAN surface did so with the selective layer (505 nm thick).

From this analysis, it is concluded that 2D quantification of surface pores by SEM provided a good estimate of pore density (effective during the filtration process) for the PES membrane. SEM images of PAN surface, however, would also include ≈25% of dead-end pores and thus, the total number of pores would be an overestimation of those which are active during the filtration process. This is an important result in the perspective of a better understanding of the water flux and then of the fouling since the actual morphology of membrane pores (open or dead-end pores) can impact this process. Surface pore density is not a sufficient parameter, especially here in the case of the PAN membrane. In order to properly relate flux of membranes obtained from microscopic measurements to macroscopic values, the amount of blind pores should probably also be included in any theoretical description of the membranes flux.

4. Conclusions

A new and detailed approach for the characterisation of UF and NF porous polymer membranes by 3D FIB/SEM is presented. This study was challenging due to the beam-sensitivity of the sample and the shine-through artefact effect occurring on these porous media. However, the

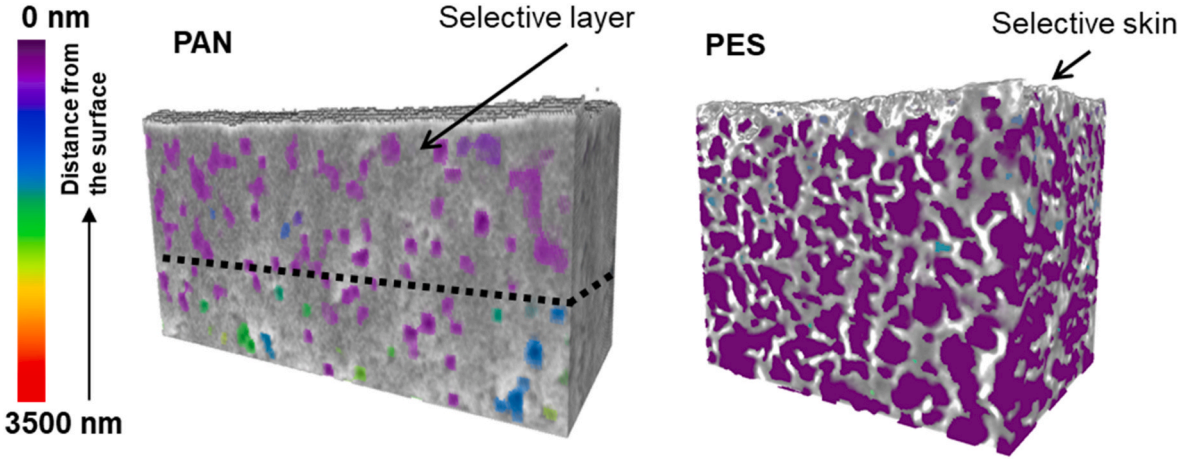

Fig. 8. Visualisation of pores connected (in purple) to the surface and going through either the selective layer or skin (open pores) of PAN and PES, respectively. Other pores starting at different depths of the membrane are indicated by different colors as shown in the scale. (For interpretation of the references to colour in this figure legend, the reader is referred to the Web version of this article.)

quality and the consistency of the 3D reconstructions of PAN and PES membranes demonstrated that, despite challenging, the electron beam sensitivity of these polymer-based membranes has been overcome. The sample preparation (dried and empty or embedded into resin) was discussed to estimate the impact on the structural properties measurement (porosity, pore diameter, selective layer thickness). The analysis of the empty membranes was selected because the shine-through artefact was limited, and the embedding led to the membrane swelling. The selective layers of PAN ultrafiltration and PES microfiltration membranes were identified. The PAN membrane presented a selective layer of 505 nm with a pore size of 30 nm while the PES membrane contained a selective skin with a pore size of 60–100 nm. Furthermore, mean pore size quantification at the membrane surface by 3D (FIB/SEM) and by 2D SEM were consistent. Finally, based on the 3D reconstructions, the percentage of blind (dead-end) pores (less than 1% for PES and 25% for PAN) were estimated, revealing that 2D SEM quantification was well suited for the PES membrane characterization while it would overestimate the operational pores for the PAN membrane. This work provided valuable data on the membrane internal structure that are crucial input for elaborate permeation models. This study of pristine membranes was a prerequisite before the study of fouled membranes by FIB/SEM could be undertaken. Another challenge will be the preservation of biomolecules, during data acquisition, within the polymer pores or at the interface cake/polymer surface. New procedures using cryogenic temperatures at the time of 3D FIB sectioning are to be developed to achieve precisely that and are currently under way. Advanced segmentation algorithms, based on deep-learning algorithms, could improve the quantification for the noisier data of this study, such as the embedded membranes or the PAN membranes and will be explored in the future.

Declaration of competing interest

The authors declare that they have no known competing financial interests or personal relationships that could have appeared to influence the work reported in this paper.

Acknowledgements

HR thanks Nicolas Stephant for his valuable help on the ZEISS crossbeam microscope and Dr Mouad Essani for useful discussions. The authors would like to thank the financial support provided by the NExT initiative through the French National Research Agency (ANR) under the Programme d'Investissements d'Avenir (with reference ANR-16-IDEX-0007). The e-BRIDGE project also receives financial support from the Pays de la Loire region and Nantes Métropole. FIB/SEM reconstructed volumes were collected in the CIMEN Electron Microscopy Center in Nantes funded by the French Contrat Plan État-Région and the European Regional Development Fund of Pays de la Loire.

Appendix A. Supplementary data

Supplementary data to this article can be found online at https://doi.org/10.1016/j.memsci.2022.120530.

References

[1] N. Rossignol, L. Vandanjon, P. Jaouen, F. Quéméneur, Membrane technology for the continuous separation microalgae/culture medium: compared performances of cross-flow microfiltration and ultrafiltration, Aquacult. Eng. 20 (1999) 191–208, https://doi.org/10.1016/S0144-8609(99)00018-7.

[2] G. Rudolph, T. Virtanen, M. Ferrando, C. Güell, F. Lipnizki, M. Kallioinen, A review of in situ real-time monitoring techniques for membrane fouling in the biotechnology, biorefinery and food sectors, J. Membr. Sci. 588 (2019) 117221, https://doi.org/10.1016/j.memsci.2019.117221.

[3] D.J. Johnson, D.L. Oatley-Radcliffe, N. Hilal, State of the art review on membrane surface characterisation: visualisation, verification and quantification of membrane properties, Desalination 434 (2018) 12–36, https://doi.org/10.1016/j.desal.2017.03.023.

[4] F. Zhao, H. Chu, Y. Zhang, S. Jiang, Z. Yu, X. Zhou, J. Zhao, Increasing the vibration frequency to mitigate reversible and irreversible membrane fouling using an axial vibration membrane in microalgae harvesting, J. Membr. Sci. 529 (2017) 215–223, https://doi.org/10.1016/j.memsci.2017.01.039.

[5] Z. Zhao, A. Ilyas, K. Muylaert, I.F.J. Vankelecom, Optimization of patterned polysulfone membranes for microalgae harvesting, Bioresour. Technol. 309 (2020) 123367, https://doi.org/10.1016/j.biortech.2020.123367.

[6] R. Huang, Z. Liu, B. Yan, Y. Li, H. Li, D. Liu, P. Wang, F. Cui, W. Shi, Layer-by-layer assembly of high negatively charged polycarbonate membranes with robust antifouling property for microalgae harvesting, J. Membr. Sci. 595 (2020) 117488, https://doi.org/10.1016/j.memsci.2019.117488.

[7] S. Liu a, I. Gifuni, H. Méar, M. Frappart, E. Couallier*, Recovery of soluble proteins from Chlorella vulgaris by bead-milling and microfiltration: impact of the concentration and the physicochemical conditions during the cell disruption on the whole process, Process Biochem. 108 (2021) 34–47, accepted.

[8] L. Villafaña-López, E. Clavijo Rivera, S. Liu, E. Couallier, M. Frappart, Shear-enhanced membrane filtration of model and real microalgae extracts for lipids recovery in biorefinery context, Bioresour. Technol. 288 (2019) 121539, https://doi.org/10.1016/j.biortech.2019.121539.

[9] E. Clavijo Rivera, L. Villafaña-López, S. Liu, R. Vinoth Kumar, M. Viau, P. Bourseau, C. Monteux, M. Frappart, E. Couallier, Cross-flow filtration for the recovery of lipids from microalgae aqueous extracts: membrane selection and performances, Process Biochem. 89 (2020) 199–207, https://doi.org/10.1016/j.procbio.2019.10.016.

[10] Y. Kourde-Hanafi, P. Loulergue, A. Szymczyk, B. Van der Bruggen, M. Nachtnebel, M. Rabiller-Baudry, J.-L. Audic, P. Pölt, K. Baddari, Influence of PVP content on degradation of PES/PVP membranes: insights from characterization of membranes with controlled composition, J. Membr. Sci. 533 (2017) 261–269, https://doi.org/10.1016/j.memsci.2017.03.050.

[11] C. Rouquié, S. Liu, M. Rabiller-Baudry, A. Riaublanc, M. Frappart, E. Couallier, A. Szymczyk, Electrokinetic leakage as a tool to probe internal fouling in MF and UF membranes, J. Membr. Sci. 599 (2020) (1 April 2020), 117707, https://doi.org/10.1016/j.memsci.2019.117707.

[12] M. Ulbricht, Advanced functional polymer membranes, Polymer 47 (2006) 2217–2262, https://doi.org/10.1016/j.polymer.2006.01.084.

[13] M. Ulbricht, O. Schuster, W. Ansorge, M. Ruetering, P. Steiger, Influence of the strongly anisotropic cross-section morphology of a novel polyethersulfone microfiltration membrane on filtration performance, Separ. Purif. Technol. 57 (2007) 63–73, https://doi.org/10.1016/j.seppur.2007.02.012.

[14] M. Mulder, J. Mulder, Basic Principles of Membrane Technology, Springer Science & Business Media, 1996.

[15] S. Habibi, M. Rabiller-Baudry, F. Lopes, F. Bellet, B. Goyeau, M. Rakib, E. Couallier, New insights into the structure of membrane fouling by biomolecules using comparison with isotherms and ATR-FTIR local quantification, Environ. Technol. (2020) 1–18, https://doi.org/10.1080/09593330.2020.1783370, 0.

[16] K.P. Brickey, A.L. Zydney, E.D. Gomez, FIB-SEM tomography reveals the nanoscale 3D morphology of virus removal filters, J. Membr. Sci. (2021) 119766, https://doi.org/10.1016/j.memsci.2021.119766.

[17] J.-C. Remigy, S. Desclaux, Filtration membranaire (OI, NF, UF) - présentation des membranes et modules, Ref TIP598WEB - Médicam. Prod. Pharm. (2007). https://www-techniques-ingenieur-fr.budistant.univ-nantes.fr/base-documentaire/42665210-production-des-medicaments-industrialisation/download/j2791/filtration-membranaire-oi-nf-uf.html. (Accessed 5 February 2021).

[18] P. Mostaghimi, M.J. Blunt, B. Bijeljic, Computations of absolute permeability on micro-CT images, Math. Geosci. 45 (2013) 103–125, https://doi.org/10.1007/s11004-012-9431-4.

[19] S. Song, L. Rong, K. Dong, X. Liu, P. Le-Clech, Y. Shen, Pore-scale numerical study of intrinsic permeability for fluid flow through asymmetric ceramic microfiltration membranes, J. Membr. Sci. 642 (2022), https://doi.org/10.1016/j.memsci.2021.119920, 119920.

[20] P. Marchetti, A. Butté, A.G. Livingston, An improved phenomenological model for prediction of solvent permeation through ceramic NF and UF membranes, J. Membr. Sci. 415–416 (2012) 444–458, https://doi.org/10.1016/j.memsci.2012.05.030.

[21] X. Chen, G. Yao, An improved model for permeability estimation in low permeable porous media based on fractal geometry and modified Hagen-Poiseuille flow, Fuel 210 (2017) 748–757, https://doi.org/10.1016/j.fuel.2017.08.101.

[22] C.-C. Ho, A.L. Zydney, Effect of membrane morphology on the initial rate of protein fouling during microfiltration, J. Membr. Sci. 155 (1999) 261–275, https://doi.org/10.1016/S0376-7388(98)00324-X.

[23] P. Aimar, P. Bacchin, A. Maurel, Filtration membranaire (OI, NF, UF, MFT) - Aspects théoriques : perméabilité et sélectivité, Ref TIP452WEB - Opérations Unit, Génie Réaction Chim., 2010. https://www-techniques-ingenieur-fr.budistant.univ-nantes.fr/base-documentaire/42331210-operations-unitaires-techniques-separatives-sur-membranes/download/j2790/filtration-membranaire-oi-nf-uf-mft.html. (Accessed 10 February 2021).

[24] M.B. Tanis-Kanbur, R.I. Peinador, J.I. Calvo, A. Hernández, J.W. Chew, Porosimetric membrane characterization techniques: a review, J. Membr. Sci. 619 (2021) 118750, https://doi.org/10.1016/j.memsci.2020.118750.

[25] L. Zou, P. Gusnawan, G. Zhang, J. Yu, Study of the effective thickness of the water-intrudable hydrophilic layer in dual-layer hydrophilic-hydrophobic hollow fiber membranes for direct contact membrane distillation, J. Membr. Sci. 615 (2020) 118552, https://doi.org/10.1016/j.memsci.2020.118552.

[26] E. Korzhova, S. Déon, Z. Koubaa, P. Fievet, D. Lopatin, O. Baranov, Modification of commercial UF membranes by electrospray deposition of polymers for tailoring physicochemical properties and enhancing filtration performances, J. Membr. Sci. 598 (2020) 117805, https://doi.org/10.1016/j.memsci.2019.117805.
[27] G. Sundaramoorthi, M. Hadwiger, M. Ben-Romdhane, A.R. Behzad, P. Madhavan, S.P. Nunes, 3D membrane imaging and porosity visualization, Ind. Eng. Chem. Res. 55 (2016) 3689–3695, https://doi.org/10.1021/acs.iecr.6b00387.
[28] J. Alvarez, G. Saudino, V. Musteata, P. Madhavan, A. Genovese, A.R. Behzad, R. Sougrat, C. Boi, K.-V. Peinemann, S.P. Nunes, 3D analysis of ordered porous polymeric particles using complementary electron microscopy methods, Sci. Rep. 9 (2019) 1–10, https://doi.org/10.1038/s41598-019-50338-2.
[29] S.P. Nunes, R. Sougrat, B. Hooghan, D.H. Anjum, A.R. Behzad, L. Zhao, N. Pradeep, I. Pinnau, U. Vainio, K.-V. Peinemann, Ultraporous films with uniform nanochannels by block copolymer micelles assembly, Macromolecules 43 (2010) 8079–8085, https://doi.org/10.1021/ma101531k.
[30] T. Terao, G. Inoue, M. Kawase, N. Kubo, M. Yamaguchi, K. Yokoyama, T. Tokunaga, K. Shinohara, Y. Hara, T. Hara, Development of novel three-dimensional reconstruction method for porous media for polymer electrolyte fuel cells using focused ion beam-scanning electron microscope tomography, J. Power Sources 347 (2017) 108–113, https://doi.org/10.1016/j.jpowsour.2017.02.050.
[31] T. Prill, C. Redenbach, D. Roldan, M. Godehardt, K. Schladitz, S. Höhn, K. Sempf, Simulating permeabilities based on 3D image data of a layered nano-porous membrane, Int. J. Solid Struct. 184 (2020) 3–13, https://doi.org/10.1016/j.ijsolstr.2019.04.010.
[32] H. Reingruber, A. Zankel, C. Mayrhofer, P. Poelt, Quantitative characterization of microfiltration membranes by 3D reconstruction, J. Membr. Sci. 372 (2011) 66–74, https://doi.org/10.1016/j.memsci.2011.01.037.
[33] M.M. Kłosowski, C.M. McGilvery, Y. Li, P. Abellan, Q. Ramasse, J.T. Cabral, A. G. Livingston, A.E. Porter, Micro-to nano-scale characterisation of polyamide structures of the SW30HR RO membrane using advanced electron microscopy and stain tracers, J. Membr. Sci. 520 (2016) 465–476, https://doi.org/10.1016/j.memsci.2016.07.063.
[34] T. Savart, Conception et réalisation de fibres creuses industrielles d'ultrafiltration en poly(fluorure de vinylidène) (PvDF) contenant des copolymères à blocs, phd, Université de Toulouse, Université Toulouse III - Paul Sabatier, 2013. http://thesesups.ups-tlse.fr/2331/. (Accessed 6 October 2021).
[35] R. Moroni, S. Thiele, FIB/SEM tomography segmentation by optical flow estimation, Ultramicroscopy 219 (2020) 113090, https://doi.org/10.1016/j.ultramic.2020.113090.
[36] H. Iwai, N. Shikazono, T. Matsui, H. Teshima, M. Kishimoto, R. Kishida, D. Hayashi, K. Matsuzaki, D. Kanno, M. Saito, H. Muroyama, K. Eguchi, N. Kasagi, H. Yoshida, Quantification of SOFC anode microstructure based on dual beam FIB-SEM technique, J. Power Sources 195 (2010) 955–961, https://doi.org/10.1016/j.jpowsour.2009.09.005.
[37] C. Rouquié, S. Liu, M. Rabiller-Baudry, A. Riaublanc, M. Frappart, E. Couallier, A. Szymczyk, Electrokinetic leakage as a tool to probe internal fouling in MF and UF membranes, J. Membr. Sci. 599 (2020) 117707, https://doi.org/10.1016/j.memsci.2019.117707.
[38] J.S. Trent, Ruthenium tetraoxide staining of polymers: new preparative methods for electron microscopy, Macromolecules 17 (1984) 2930–2931, https://doi.org/10.1021/ma00142a087.
[39] W. Chen, M. Zhu, S. Song, B. Sun, Y. Chen, H.-J.P. Adler, Morphological characterization of PMMA/PAN composite particles in nano to submicro size, Macromol. Mater. Eng. 290 (2005) 669–674, https://doi.org/10.1002/mame.200400291.
[40] E. Por, M. van Kooten, V. Sarkovic, Nyquist–Shannon Sampling Theorem, (n.d.) 4.
[41] S. Qi, W. Fang, W. Siti, W. Widjajanti, X. Hu, R. Wang, Polymersomes-based high-performance reverse osmosis membrane for desalination, J. Membr. Sci. 555 (2018) 177–184, https://doi.org/10.1016/j.memsci.2018.03.052.
[42] B. Kuei, M.P. Aplan, J.H. Litofsky, E.D. Gomez, New opportunities in transmission electron microscopy of polymers, Mater. Sci. Eng. R Rep. 139 (2020) 100516, https://doi.org/10.1016/j.mser.2019.100516.
[43] R.F. Egerton, Radiation damage to organic and inorganic specimens in the TEM, Micron 119 (2019) 72–87, https://doi.org/10.1016/j.micron.2019.01.005.
[44] Dragonfly | 3D visualization and analysis solutions for scientific and industrial data | ORS (n.d.), https://www.theobjects.com/index.html. (Accessed 7 October 2021).
[45] F.D.E. Latief, Analysis and visualization of 2D and 3D grain and pore size of Fontainebleau sandstone using digital rock physics, J. Phys. Conf. Ser. 739 (2016), 012047, https://doi.org/10.1088/1742-6596/739/1/012047.
[46] R. Kumar, A.M. Isloor, A.F. Ismail, T. Matsuura, Performance improvement of polysulfone ultrafiltration membrane using N-succinyl chitosan as additive, Desalination 318 (2013) 1–8, https://doi.org/10.1016/j.desal.2013.03.003.
[47] J. Ge, Q. Jin, D. Zong, J. Yu, B. Ding, Biomimetic multilayer nanofibrous membranes with elaborated superwettability for effective purification of emulsified oily wastewater, ACS Appl. Mater. Interfaces 10 (2018) 16183–16192, https://doi.org/10.1021/acsami.8b01952.
[48] F. Liu, M.R.M. Abed, K. Li, Hydrophilic modification of P(VDF-co-CTFE) porous membranes, Chem. Eng. Sci. 66 (2011) 27–35, https://doi.org/10.1016/j.ces.2010.09.026.